

CONSTRAINTS ON THE SHAPE OF THE MILKY WAY DARK MATTER HALO FROM THE SAGITTARIUS STREAM

CARLOS VERA-CIRO^{1,2} & AMINA HELMI²
Draft version October 6, 2018

ABSTRACT

We propose a new model for the dark matter halo of the Milky Way that fits the properties of the stellar stream associated with the Sagittarius dwarf galaxy. Our dark halo is oblate with $q_z = 0.9$ for $r \lesssim 10$ kpc, and follows the Law & Majewski (2010) model at large radii, the transition between these regimes occurring at ~ 30 kpc. The outer halo can be made mildly triaxial, with minor-to-major axis ratio $(c/a)_\phi = 0.8$ and intermediate-to-major axis ratio $(b/a)_\phi = 0.9$, if the effect of the Large Magellanic Cloud is taken into account. Therefore this new model takes into account the flattening induced by the presence of the Galactic disk and is also more consistent with cosmological expectations.

Subject headings: galaxies: dwarf – galaxies: interactions – Local Group – Galaxy: halo

1. INTRODUCTION

The stellar stream associated with the Sagittarius (Sgr) dwarf galaxy has been extensively used to probe the mass distribution of the Milky Way (MW), particularly its dark halo. Despite many attempts, there is currently no fully satisfactory model of its shape based the dynamics of the stream. Extreme oblate configurations have been ruled out (Ibata et al. 2001), while the tilt of the orbital plane has been shown to require a mildly oblate halo by Johnston, Law & Majewski (2005). On the other hand, the line of sight velocities call for a prolate halo (Helmi 2004). This conundrum led (Law & Majewski 2010, hereafter LM10) to propose a triaxial dark halo for the MW, with axis ratios $(c/a)_\phi = 0.72$ and $(b/a)_\phi = 0.99$ (see also Deg & Widrow 2012). This model fits well all positional and kinematic information available.

Although the halos assembled in Λ CDM are as a rule triaxial (Jing & Suto 2002; Allgood et al. 2006; Schneider, Frenk & Cole 2012), the configuration proposed by LM10 is rare: the halo is close to oblate, with a much smaller c/a than predicted in cosmological simulations for MW-mass halos, which have $\langle c/a \rangle_\phi = 0.9 \pm 0.1$ over the relevant distance range (Hayashi, Navarro & Springel 2007), and difficult to understand from a physical point of view (its minor axis points almost towards the Sun, while the intermediate axis is perpendicular to the Galactic disk). Furthermore, the presence of the disk is expected to lead to a change in the inner halo shape towards a more oblate configuration (Bryan et al. 2013). Finally, the disk's stability is not naturally ensured in the LM10 potential, as there are no tube orbits around the intermediate axis (Debattista et al. 2013).

In this *Letter* we take a fresh look at determining the shape of the MW halo from the Sgr streams dynamics. We consider the possibility that the shape of the halo varies with distance from the Galactic center, as expected in the context of Λ CDM (Vera-Ciro et al. 2011). Evidence suggesting a halo with non-constant axis ratios has been reported by Banerjee & Jog (2011) using the flaring of the HI layer of the MW disk. We present a new model that takes into account the effect of a baryonic disk in Section 2. Because of the cosmological rareness of the LM10 model, in Sec. 3 we explore the possibility that the dynamics of the Sgr stream may be explained through the combined effect

of the Large Magellanic Cloud (LMC) and a less axisymmetric, but more triaxial, outer halo. In that section we show that these models provide equally good fits to the dynamics of the young Sgr streams as the LM10 potential, and that older wraps may be used to distinguish amongst them. We finalize with a brief summary in Sec. 4.

2. INNER HALO: ACCOUNTING FOR THE EFFECT OF THE GALACTIC DISK ON THE HALO SHAPE

Next we present the characteristics of our Galactic potential, which includes a halo whose shape by construction, is oblate in the center, and triaxial at large radii. We then show the results of orbital integrations in this potential aimed at reproducing the properties of the Sgr stream.

2.1. Description of the potential

We model the Galactic potential with three components: a disk, a spherical bulge and a dark matter halo. The disk and bulge follow, respectively a Miyamoto-Nagai distribution ($M_{\text{disk}} = 10^{11} M_\odot$, $a = 6.5$ kpc, $b = 0.26$ kpc, Miyamoto & Nagai 1975), and a Hernquist spheroid ($M_{\text{bulge}} = 3.4 \times 10^{10} M_\odot$, $c = 0.7$ kpc, Hernquist 1990).

Based on the arguments presented in the Introduction, we seek a halo potential that satisfies:

1. It is axisymmetric in the inner parts. This will guarantee the stability of the disk, as well as account for the effects of the baryonic disk on the dark halo.
2. It is triaxial in the outskirts, and follows the LM10 model.
3. It has a smooth transition between these two regimes.

We choose to model such a profile using a modification of the algorithm presented by Vogelsberger et al. (2008). Consider the spherical potential

$$\Phi_s(r) = v_{\text{halo}}^2 \ln(r^2 + d^2). \quad (1)$$

The geometrical properties of the potential are encapsulated in the variable $r = (x^2 + y^2 + z^2)^{1/2}$. A replacement that satisfies the above requirements is $r \rightarrow \tilde{r}$, with

$$\tilde{r} \equiv \frac{r_a + r_T}{r_a + r_A} r_A. \quad (2)$$

Note that for $r \ll r_a$ $\tilde{r} \approx r_A$, and similarly $r \gg r_a$ $\tilde{r} \approx r_T$. If r_A is therefore defined as a quantity with axial symmetry, a

² Department of Astronomy, University of Wisconsin, 2535 Sterling Hall, 475 N. Charter Street, Madison, WI 53076, USA. e-mail: ciro@astro.wisc.edu

² Kapteyn Astronomical Institute, University of Groningen, P.O.Box 800, 9700 AV Groningen, The Netherlands.

potential of the form $\Phi_s(\tilde{r})$ will behave axisymmetrically for $r \ll r_a$. The properties of the mass distribution for $r \gg r_a$ are encoded in the quantity r_T which we define the same way as LM10. In summary,

$$r_A^2 \equiv x^2 + y^2 + \frac{z^2}{q_z^2} = R^2 + \frac{z^2}{q_z^2}, \quad (3)$$

$$r_T^2 \equiv C_1 x^2 + C_2 y^2 + C_3 xy + \frac{z^2}{q_3^2}, \quad (4)$$

and,

$$C_1 = \frac{a_1^2}{q_1^2} + \frac{a_2^2}{q_2^2}, \quad C_2 = \frac{a_1^2}{q_2^2} + \frac{a_2^2}{q_1^2}, \quad C_3 = 2a_1 a_2 \left(\frac{1}{q_1^2} - \frac{1}{q_2^2} \right), \quad (5)$$

where $a_1 = \cos \phi$ and $a_2 = \sin \phi$ and $\phi = 97^\circ$. The Sun is assumed to be located along the x axis, at $x = -R_\odot$, and the z axis to point perpendicular to the disk. The resulting potential

$$\Phi_{\text{halo}}(x, y, z) = \Phi_s(\tilde{r}(x, y, z)), \quad (6)$$

is axisymmetric for $r \ll r_a$, and triaxial for $r \gg r_a$.

Fig. 1 shows different slices of the resulting potential. Here we have chosen the flattening of the axisymmetric part to be $q_z = 0.9$ (as in e.g. Johnston, Law & Majewski 2005). The axis ratios for the triaxial component (q_1, q_2, q_3), as well as its tilt ϕ , are taken from the LM10 model. The circular velocity v_{halo} is set to ensure that $v_{\text{circ}}(R_\odot = 8 \text{ kpc}) = 225.2 \text{ km s}^{-1}$. The transition radius $r_a = 30 \text{ kpc}$, is selected such that the region of dominance of the disk resides inside the axisymmetric part of the halo potential. However, the effective transition between the axisymmetric and triaxial regions, occurs at a smaller radius, $\approx 10 \text{ kpc}$.

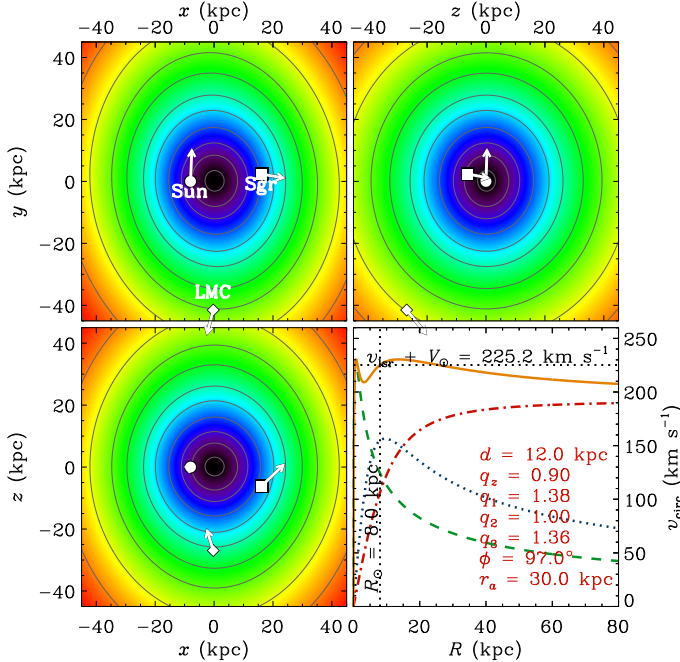


FIG. 1.— Dark halo potential isocontours on the plane $z = 0$ (top left), $y = 0$ (bottom left) and $x = 0$ (top right). For reference we have included the positions and directions of motion for the Sun (circle), Sgr (square) and the LMC (diamond). The bottom right panel shows the circular velocity profile v_{circ} for the disk (dotted blue), bulge (dashed green) and halo (dash dotted red). The halo makes a transition from oblate to triaxial at $r_a = 30 \text{ kpc}$.

2.2. Generating the stream

In what follows we work on the assumption that the orbit of the center of mass traces the arms of the stream. Although this is not strictly true (Eyre & Binney 2009), it represents a reasonable first approximation (Law & Majewski 2010). With this caveat, we proceed to integrate test particles in the composite potential described above. For each particle we generate a set of initial conditions consistent with the present day six dimensional phase-space coordinates of the Sgr dwarf galaxy. More specifically, we sample each observable from a Gaussian distribution, with its mean and variance taken from the literature. The position is assumed to be at $(l, b) = (5.6^\circ, -14.2^\circ)$ (Majewski et al. 2003), the heliocentric distance $d = 25 \pm 2 \text{ kpc}$ (Kunder & Chaboyer 2009), the line of sight velocity $v_r = 140 \pm 2 \text{ km s}^{-1}$ (Ibata et al. 1997) and the proper motions $(\mu_l \cos b, \mu_b) = (-2.4 \pm 0.2, 2.1 \pm 0.2) \text{ mas yr}^{-1}$ (Dinescu et al. 2005). Orbits are integrated forward and backward in time for 2 Gyr, to generate the set of observables associated with the leading and trailing arm, respectively.

For each integrated orbit, we take 10 samples of the form $\{\mathbf{x}(t_i), \mathbf{v}(t_i)\}_{i=1}^{10}$, where the times t_i are randomly selected between $t = 0$ and the maximum time of integration t_{max} . t_{max} is the time that it takes the orbit to complete one wrap in the sky, and is typically $\sim 1 \text{ Gyr}$. The full 6D information contained in each sample is transformed into the set of observables often used to represent the stream: position on the sky (Λ_\odot, B_\odot) (Majewski et al. 2003), heliocentric distance d , line-of-sight velocity in the Galactic standard of rest v_{gsr} , and proper motions $(\mu_b, \mu_l \cos b)$.

In total 5×10^4 initial conditions are integrated, producing 5×10^5 points in the space of observables, which are assigned to a grid using the Cloud in Cell algorithm (Hockney & Eastwood 1988). Fig. 2 shows the projected density for different observables as a function of the angular coordinate Λ_\odot : $P(o, \Lambda_\odot)$, with $o = \{v_{\text{gsr}}, B_\odot, d, \mu_b, \mu_l \cos b\}$. In each panel we marginalize the density over the observed quantity o at fixed Λ_\odot , that is $P(o|\Lambda_\odot) = \int do P(o, \Lambda_\odot)$. The solid black line shows the median of $P(o|\Lambda_\odot)$, and with gray bands we represent the 1 and 2σ equivalent scatter around the median.

For comparison we have included the mean orbit of the LM10 model (orange dashed line), and their N -body run (green dots). We have also added the measurements of Majewski et al. (2004) (cyan stars), Correnti et al. (2010) (magenta triangles) and Carlin et al. (2012) (red diamonds). As mentioned before, there are some deviations between the mean orbit and the location of the tidal stream as probed by the N -body run, for example in the distances d of the trailing arm.

Fig. 2 shows that the radial velocities v_{gsr} , distances and the positions in the sky B_\odot are well fit in our new potential, and as well as in the LM10 model. In test runs we found that the dependence of the fits on the parameter r_a is not strong, whenever this is kept within reasonable values. Of course, a value of $r_a \gg r_{\text{apo}}$ will lead to potential that is purely oblate in the region probed by the stream, and therefore will not be able to fit the velocities of the leading arm.

The dependence on the flattening q_z is shown in Fig. 3 for the leading arm (the trailing arm is rather insensitive in the region where observations are available). We explore four different values of $q_z = \{0.7, 0.8, 0.9, 1.1\}$ keeping $r_a = 30 \text{ kpc}$. In the regions probed by the data, $\Lambda_\odot \gtrsim 200^\circ$, the effect of changing q_z is strong on the velocities, which clearly rule out $q_z < 0.9$. On the other hand, the positions on the sky disfavor

$q_z > 1$. In general, we find that $0.90 < q_z < 0.95$ yield good fits to the observables in the leading arm.

3. OUTER HALO: THE EFFECT OF LMC

It is very intriguing that the direction of the major axis of the LM10 potential approximately lies in the direction towards the LMC. This suggests that the LM10 potential may perhaps be seen as an effective field: the result of the combined potentials of the LMC and of a truly triaxial MW halo.

Let us consider the various torques exerted on the (instantaneous) plane of motion of Sgr. First, note that since $\phi \approx 90^\circ$, the principal axes of the potential of the halo are nearly aligned with the Galactocentric coordinate system. Consequently, we can simplify Eq. (4) to

$$\tilde{r}^2 \approx x^2 + \frac{y^2}{q_1^2} + \frac{z^2}{q_3^2}. \quad (7)$$

The torque induced by the LM10 potential is simply $\boldsymbol{\tau} = -\mathbf{r} \times \partial\Phi_{\text{halo}}/\partial\mathbf{r}$. Of the three components of this field, the x and y components are controlled by gradient of the force along the z direction, i.e. that of the major axis of the LM10 halo. Consider for instance the z component,

$$\begin{aligned} \tau_z^{\text{halo}} &= -\frac{\partial\Phi_{\text{halo}}}{\partial\tilde{r}} \frac{xy}{\tilde{r}} \left(\frac{1}{q_1^2} - 1 \right) \approx -\frac{v_{\text{circ}}^2}{\tilde{r}^2} xy \left(\frac{1}{q_1^2} - 1 \right) \\ &\approx -\frac{GM_{\text{halo}}(\tilde{r})}{\tilde{r}^3} xy \left(\frac{1}{q_1^2} - 1 \right). \end{aligned} \quad (8)$$

Note that in our reference system the present day position of the LMC is nearly on the plane $x = 0$ (See Fig. 1). The force generated at $\mathbf{r} = x\mathbf{i} + y\mathbf{j} + z\mathbf{k}$ by a point mass M_{LMC} at the

position of the LMC, \mathbf{r}_{LMC} , is

$$\mathbf{F}_{\text{LMC}} = -GM_{\text{LMC}} \frac{\mathbf{r} - \mathbf{r}_{\text{LMC}}}{|\mathbf{r} - \mathbf{r}_{\text{LMC}}|^3}, \quad (9)$$

that generates a torque $\boldsymbol{\tau}^{\text{LMC}} = \mathbf{r} \times \mathbf{F}_{\text{LMC}}$, whose z component is

$$\tau_z^{\text{LMC}} = -\frac{GM_{\text{LMC}}}{|\mathbf{r} - \mathbf{r}_{\text{LMC}}|^3} (yx_{\text{LMC}} - xy_{\text{LMC}}) \approx \frac{GM_{\text{LMC}} xy_{\text{LMC}}}{|\mathbf{r} - \mathbf{r}_{\text{LMC}}|^3}. \quad (10)$$

Using Eqs. (8) and (10) we can quantify the relative amplitude of the torques exerted by the triaxial halo and by the LMC on the orbit of Sgr at its present location

$$\frac{\tau_z^{\text{LMC}}}{\tau_z^{\text{halo}}} \sim \frac{M_{\text{LMC}}}{M_{\text{halo}}(\tilde{r})} \frac{\tilde{r}^3}{r_{\text{sgr/LMC}}^3} \frac{y_{\text{LMC}}}{y} \frac{1}{1/q_1^2 - 1}. \quad (11)$$

The mass of the LM10 halo enclosed at the present distance of Sgr is $M_{\text{halo}} \sim 10^{11} M_\odot \approx M_{\text{LMC}}$ (Besla et al. 2010). At the present day $\tilde{r}/r_{\text{sgr/LMC}} \sim 0.5$, while $y_{\text{LMC}}/y \sim 10$, and taking $q_1 = 1.38$, this implies that the expression above is of order unity. Additionally, since $q_1 > 1$ the torque generated by the LMC points in the same direction of that induced by the triaxial halo ($y_{\text{LMC}} < 0$, c.f. Fig. 1). This means that presently the torque on Sgr generated by the LMC is as important as the one generated by the triaxial halo.

To confirm this order of magnitude argument we perform new orbital integrations in a slightly modified halo model, which is still given by Eq. (6) but now with axis ratios $q_1 = 1.1$, $q_2 = 1.0$ and $q_3 = 1.25$, and where we have kept the orientation $\phi = 97^\circ$. We also include the potential of the LMC. To this end, we evolve backward and forward the orbit of the LMC, from its present day position $(\alpha, \delta) = (5^{\text{h}}, 27.^\text{m}6, -69^\circ, 52.2')$ (Piatek, Pryor & Olszewski 2008), heliocentric distance $d = 50.1$ kpc (Freedman et al. 2001), proper motions $(\mu_l \cos b, \mu_b) = (1.96, 0.44)$ mas yr $^{-1}$ (Piatek, Pryor & Olszewski 2008) and line-of-sight velocity $v_r = 270$ km s $^{-1}$ (van der Marel et al.

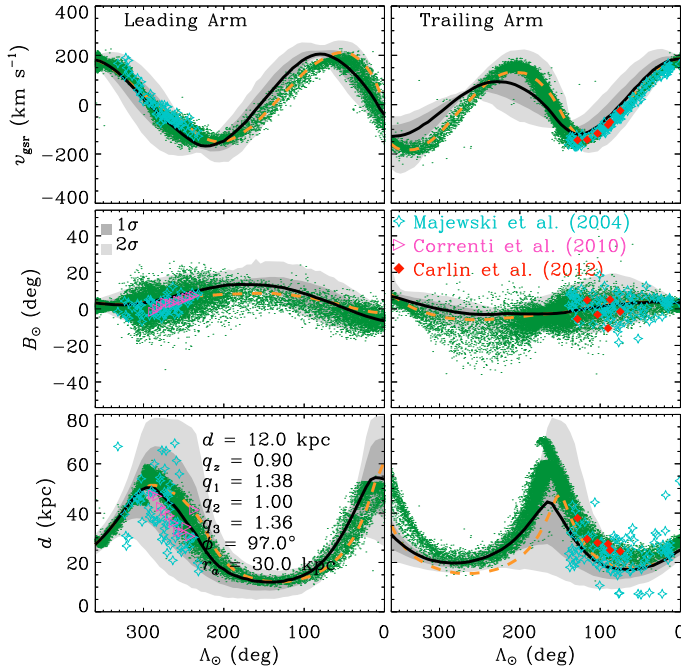


FIG. 2.— Radial velocity v_{sgr} , position in the sky B_\odot , and heliocentric distance d as function of the angular distance along the stream Λ_\odot for the leading arm (left) and trailing arm (right) for the potential described in Fig. 1. The solid black line is the median orbit and the shaded regions represent 1σ and 2σ equivalent dispersion. The green points are from the N -body simulation by LM10, while their center of mass orbit is the orange dashed curve.

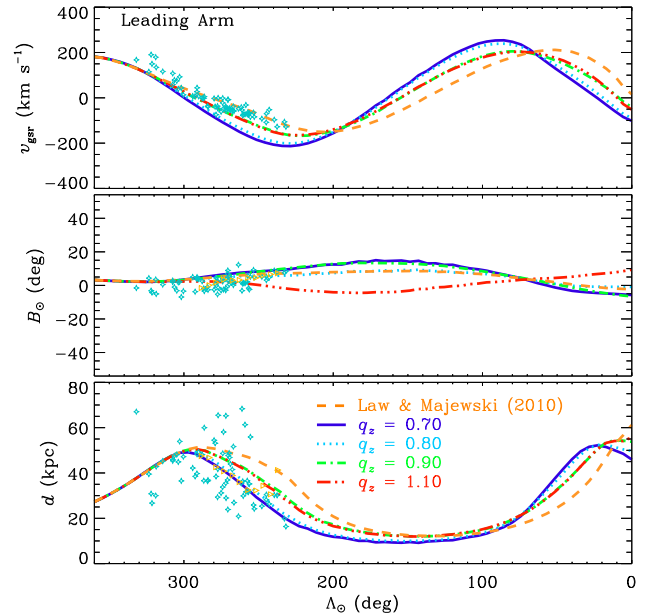


FIG. 3.— Leading arm line-of-sight velocities (top), position on the sky (middle) and heliocentric distances (bottom) for different q_z and $r_a = 30$ kpc. The potential for $r \gg r_a$ is the same triaxial model as in Fig. 2. The dashed orange line is the mean orbit of LM10.

2002). We then place a Hernquist sphere of mass $M_{\text{LMC},0} = 8 \times 10^{10} M_{\odot}$ and scale radius $r_{\text{LMC},0} = 2$ kpc along this orbit.

Fig. 4 shows a model of the Sgr stream orbital path in which the LMC and our slightly revised halo are included. As before we show the LM10 model with the dashed orange line. It is interesting to note that after including the LMC in our model, the orbital tilt of the leading arm is well fit despite the change in shape of the MW halo, which is now elongated in the z -direction at large radii. The torque of the orbital plane is, of course, also felt by the trailing arm, resulting on a slight change in the direction of gradient of B_{\odot} for $\Lambda \lesssim 100^{\circ}$.

This analysis shows that the perturbations of the LMC on the orbit of the Sgr stream are non-negligible. In a more realistic scenario including dynamical friction, the LMC might have been even more massive than at present day, and as a consequence, its role in shaping the orbit of Sgr even more important. However, some caution is necessary before drawing strong conclusions about the dynamics of the stream 3-4 Gyr ago. For example, if the LMC is in its first infall, in which case the closest encounter with the Sgr dwarf galaxy is currently taking place. However, during the last ~ 2 Gyr its presence could have significantly affected older wraps of the Sgr stream.

We explore in Fig. 5 how the differences between the various models may become apparent for older portions of the stream. Here we show the first (solid line) and second (dotted line) wraps of the leading (left) and trailing (right) arms, for the three different models discussed so far: black is our fiducial model from Section 2, green is the model that includes the LMC and red is the LM10 triaxial model. We have included observations of different stellar tracers: RR Lyraes (Ivezić et al. 2000; Vivas, Zinn & Gallart 2005; Prior, Da Costa & Keller 2009), Car-

bon Giants (Ibata et al. 2001), RGB stars (Dohm-Palmer et al. 2001; Starkenburg et al. 2009; Correnti et al. 2010), M Giants (Majewski et al. 2004) and Red Horizontal Branch stars (Shi et al. 2012). It should be noted that (Shi et al. 2012) preselect their sample according to the LM10 model.

We show also the positions in the sky for the bright (orange filled squares) and the faint (orange open squares) streams in the Southern Galactic hemisphere from Koposov et al. (2012). Whereas the association to the trailing arm is clear for the brighter portion of the stream, the faint parallel stream could perhaps be an older wrap from either trailing or leading arm. More information, especially kinematic is necessary to disentangle the various contributions of Sgr in this region of the sky, and these might also help constrain further the shape of the dark halo of the Milky Way. It should be born in mind that although the differences between older wraps amongst the various models are larger than for younger streams, the predictions for their properties are clearly much more uncertain.

4. CONCLUSIONS

In this paper we have presented a new model for the MW dark matter halo that fits the observations of the Sgr stream, both the radial velocities as well as the orbital tilt of the leading arm. The dark halo potential is axisymmetric and flattened towards the disk plane for $r \lesssim 10$ kpc, with $q_z = 0.9$, and asymptotically approaches the Law & Majewski (2010) triaxial model at larger radii. A gratifying property of this potential is that its inner oblate shape and orientation account for the presence of the Galactic disk and ensure its stability.

The triaxial part of this potential, however is not entirely consistent with expectations from the Λ CDM model. Its odd (nearly oblate) configuration can be changed, and brought to a more cosmologically plausible shape, if the gravitational field generated by the Large Magellanic Cloud is taken into account. The integration of orbits in a composite potential including the LMC and an outer triaxial halo with $q_1 = 1.10$, $q_2 = 1.00$ and $q_3 = 1.25$ (that is as before, oblate in the inner regions), is also found to reproduce well the properties of the Sgr streams in the region where these have been constrained observationally.

The conclusions drawn in this work are based on heuristic searches of the high-dimensional parameter space that characterizes the gravitational potential of the Milky Way and that of the LMC. By no means do they represent best fit models in a statistical sense. Therefore, the predictions made cannot be considered exclusive or definitive, but serve to guide where future observations could focus to distinguish between various models. Notwithstanding these caveats, we have been able to demonstrate that the dynamics of the Sgr streams can be understood in a context that is consistent with expectations from the Λ CDM model.

ACKNOWLEDGMENTS

We are grateful to Laura V. Sales and Shoko Jin for useful discussions, and acknowledge financial support from the European Research Council under ERC-StG grant GALACTICA-24027.

REFERENCES

Allgood B., Flores R. A., Primack J. R., Kravtsov A. V., Wechsler R. H., Faltenbacher A., Bullock J. S., 2006, MNRAS, 367, 1781

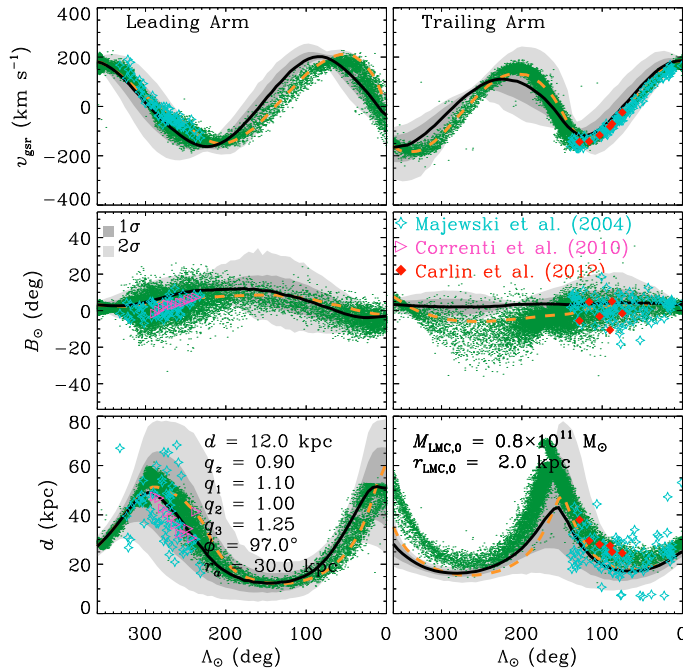


FIG. 4.— Radial velocity v_{sgr} , position in the sky B_{\odot} , heliocentric distance d and proper motions $\mu_l \cos b, \mu_b$ as a function of the angular distance along the stream Λ_{\odot} for the leading arm (left) and trailing arm (right). The potential used includes the LMC as well as that for the halo, which has the form described in Eqs. (2)–(6), i.e. it is oblate in the center with $q_z = 0.9$ and $r_a = 30$ kpc, but with axis ratios $q_1 = 1.1$, $q_2 = 1.0$ and $q_3 = 1.25$.

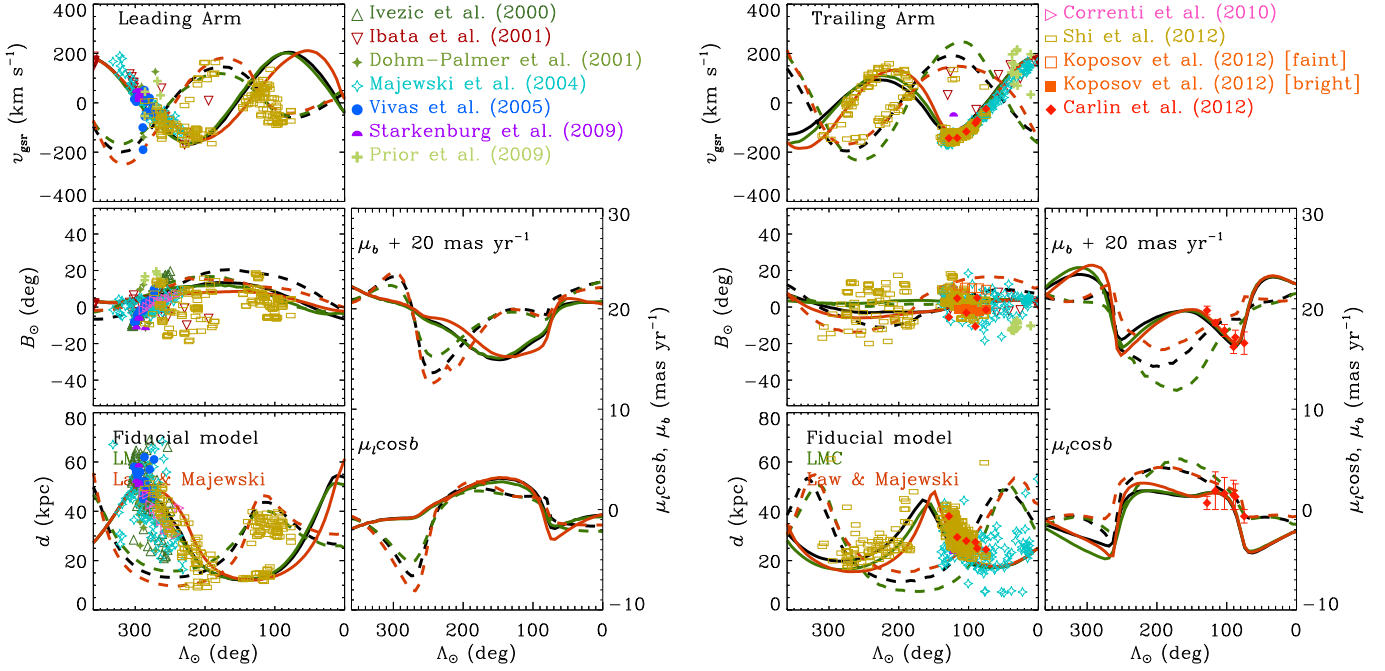


FIG. 5.— First and second wraps of the leading and trailing streams from Sgr for the different models explored: black is our fiducial model from Section 2, green is the model that includes the LMC and red is the LM10 triaxial model.

Banerjee A., Jog C. J., 2011, *ApJ*, 732, L8
Besla, G. and Kallivayalil, N. and Hernquist, L. and van der Marel, R. P. and Cox, T. J. and Kereš, D., 2010, *ApJ*, 721, 97
Bryan S. E., Kay S. T., Duffy A. R., Schaye J., Dalla Vecchia C., Booth C. M., 2013, *MNRAS*, 429, 3316
Carlin J. L., Majewski S. R., Casetti-Dinescu D. I., Law D. R., Girard T. M., Patterson R. J., 2012, *ApJ*, 744, 25
Correnti M., Bellazzini M., Ibata R. A., Ferraro F. R., Varghese A., 2010, *ApJ*, 721, 329
Debatista V. P., Roskar R., Valluri M., Quinn T., Moore B., Wadsley J., 2013, *arXiv:1301.2670*
Deg N., Widrow L., 2012, *MNRAS*, 428, 912
Dinescu D. I., Girard T. M., van Altena W. F., López C. E., 2005, *ApJ*, 618, L25
Dohm-Palmer R. C. et al., 2001, *ApJ*, 555, L37
Eyre A., Binney J., 2009, *MNRAS*, 400, 548
Freedman W. L. et al., 2001, *ApJ*, 553, 47
Hayashi E., Navarro J. F., Springel V., 2007, *MNRAS*, 377, 50
Helmi A., 2004, *ApJ*, 610, L97
Hernquist L., 1990, *ApJ*, 356, 359
Hockney R. W., Eastwood J. W., 1988, *Computer simulation using particles*. Taylor & Francis
Ibata R., Lewis G. F., Irwin M., Totten E., Quinn T., 2001, *ApJ*, 551, 294
Ibata R. A., Wyse R. F. G., Gilmore G., Irwin M. J., Suntzeff N. B., 1997, *AJ*, 113, 634
Ivezić Ž. et al., 2000, *AJ*, 120, 963
Jing Y. P., Suto Y., 2002, *ApJ*, 574, 538
Johnston K. V., Law D. R., Majewski S. R., 2005, *ApJ*, 619, 800
Koposov S. E. et al., 2012, *ApJ*, 750, 80
Kunder A., Chaboyer B., 2009, *AJ*, 137, 4478
Law D. R., Majewski S. R., 2010, *ApJ*, 714, 229 (LM10)
Majewski S. R., Skrutskie M. F., Weinberg M. D., Ostheimer J. C., 2003, *ApJ*, 599, 1082
Majewski S. R. et al., 2004, *AJ*, 128, 245
Miyamoto M., Nagai R., 1975, *PASJ*, 27, 533
Piatek S., Pryor C., Olszewski E. W., 2008, *AJ*, 135, 1024
Prior S. L., Da Costa G. S., Keller S. C., 2009, *ApJ*, 704, 1327
Starkenburg E. et al., 2009, *ApJ*, 698, 567
Schneider M. D., Frenk C. S., Cole S., 2012, *J. Cosmology Astropart. Phys.*, 5, 30
Shi W. B., Chen Y. Q., Carrell K., Zhao G., 2012, *ApJ*, 751, 130
van der Marel, R. P. and Alves, D. R. and Hardy, E. and Suntzeff, N. B., 2002, *ApJ*, 124, 2639
Vera-Ciro C. A., Sales L. V., Helmi A., Frenk C. S., Navarro J. F., Springel V., Vogelsberger M., White S. D. M., 2011, *MNRAS*, 416, 1377
Vivas A. K., Zinn R., Gallart C., 2005, *AJ*, 129, 189
Vogelsberger M., White S. D. M., Helmi A., Springel V., 2008, *MNRAS*, 385, 236